Model-data-driven image reconstruction with neural networks for ultrasound computed tomography breast imaging

Yuling Fan [a], Hongjian Wang [b,*], Hartmut Gemmeke [c], Torsten Hopp [c], Juergen Hesser [a]

[a] Heidelberg University, Mannheim, Germany
[b] School of Computer Science and Technology, Donghua University, Shanghai, China
[c] Karlsruhe Institute of Technology, Karlsruhe, Germany

ARTICLE INFO

Keywords:
Breast cancer
Ultrasound computed tomography
Deep learning
Image reconstruction

ABSTRACT

With the goal of developing an accurate and fast image reconstruction algorithm for *ultrasound computed tomography*, we combine elements of model- and data-driven approaches and propose a learned method which addresses the disadvantages of both approaches. We design a deep neural network which accounts for a nonlinear forward operator and primal-dual algorithm by its inherent network architecture. The network is trained end-to-end, with ultrasound pressure field data as input to get directly an optimized reconstruction of speed of sound and attenuation images. The training and test data are based on a set of *Optical and Acoustic Breast Phantom Database*, where we use the image as ground truth and simulate pressure field data according to our forward model. Extensive experiments show that our method achieves significant improvements over state-of-the-art reconstruction methods in this field. Experiments show that the proposed algorithm improves the measures structural similarity measure (SSIM) from 0.74 to 0.95 and root mean squared error (RMSE) from 0.13 to 0.09 on average concerning the speed of sound reconstruction, while it improves the SSIM from 0.60 to 0.94 and RMSE from 0.24 to 0.10 on average in attenuation reconstruction.

1. Introduction

Ultrasound computed tomography (USCT) promises high specificity for early breast cancer detection without the associated risks of ionizing radiation while with lower costs than magnetic resonance tomography. It images the reflectivity, speed of sound (SoS) and attenuation of breast tissue. USCT devices allow to observe reflection and transmission tomography at the same time [1]. Yet, the widespread use of high-quality USCT is mainly limited by the excessive time for image reconstruction, which prevents currently the application of sophisticated reconstruction techniques within clinical workflows. Hence, there is an urgent need in fast and accurate reconstruction methods.

The simplified relationship of USCT between SoS, attenuation and breast tissue types is shown in Fig. 1. Both in combination of SoS and attenuation are expected to be a discriminator for different tissue types and also to distinguish malign and benign lesions [2]. The goal of USCT image reconstruction is to reconstruct SoS and attenuation, which are incorporated in a complex variable η that describes the deviation of SoS and attenuation in the breast from the background medium of water [1].

The inverse problem of image reconstruction can be formulated as reconstruction of the inhomogeneity (ground truth) $\eta_{true} \in X$ from ultrasound pressure field data (frequency data) $p \in Y$ measured from the USCT system, where

$$p = \mathbf{T}(\eta_{true}) + \delta p \tag{1}$$

Here, X is the image domain; Y is the frequency domain; $\delta p \in Y$ denotes the noise in the frequency data; the forward operator $\mathbf{T} : X \to Y$ models how the ground truth gives rise to frequency data.

Recently, deep learning (DL) seems to offer new potentials in solving ill-posed inverse problems. Compared with traditional optimization-based algorithms, once learned, the inverse operators yield impressive reconstruction performance. Yet, the learning process is the Archilles' heel of these techniques since the larger the data dimension is, the larger should be the necessary learning data for being rich enough to account for accurate mapping.

Many algorithms based on deep neural networks (DNNs) have been used for computed tomography (CT) image reconstruction. In particular, a convolutional encoder-decoder (CED) architecture [4] has been readily available for CT image reconstruction. The

* Corresponding author.
E-mail address: hongjian.wang@dhu.edu.cn (H. Wang).

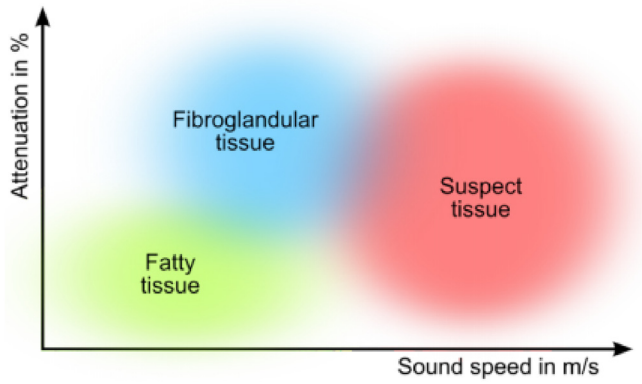

Fig. 1. Simplified relationship between SoS, attenuation and breast tissue types [3].

CED has been used to restore high-quality CT images from low dose CT images. Han et al. [5] propose a deep residual learning network for sparse view CT reconstruction via persistent homology analysis. Jin et al. [6] propose a filtered back projection conversion network (FBPConvNet) architecture which combines filtered back projection and U-net architecture to improve the image quality. In [7], a DD-Net based on DenseNet and deconvolution is developed to accelerate the network training speed.

However, using DL to reconstruct USCT images is rarely found in literature compared to CT reconstruction. From the mathematical side, the main difference is that CT can be well approximated by straight rays whereas USCT is a typical example of wave and scatter tomography, both complications that make standard CT reconstruction and other image reconstruction methods with DL not usable and pose severe problems in the reconstruction algorithms. It is a good starting point to mention the CT deep learning reconstruction as a motivation, but we cannot learn so much for USCT due to its wave properties (refraction, diffraction and scattering).

In this paper, we design a novel DNN architecture based on a primal–dual method [8] to obtain both fast and high-quality image reconstruction as a major breakthrough for these ultrasound applications. It maps the traditional primal-dual algorithm [8] into a dual-domain (pressure field frequency domain and image domain) network architecture for optimizing a general USCT image reconstruction model with a DNN.

In the traditional primal-dual hybrid gradient (PDHG) methods [8–10], a forward model and its adjoint are needed for the computation of each iteration. However, the forward model for USCT requires solving a wave equation [1,11], which is a highly computational burden. In addition, computing the adjoint is time-consuming as well. Therefore, we replace the adjoint by our frequency-to-image domain network (FI-Net) architecture. Our network unrolls a fixed number of iterations of a primal-dual optimization strategy, where in each iteration a convolutional neural network (CNN) is applied for both frequency domain and image domain. Iterations are connected by both the forward operator and the FI-Net. In particular, in the image domain, nonlinear transforms are learned instead of learning traditional linear transforms. Furthermore, our network can be seen as an attempt to build a bridge between the model-based and data-based methods.

To gain substantial improvements and address above problems, we make the following contributions:

- The network is able to reconstruct images without any initial reconstruction such as filtered back-projection (FBP) and use CNNs to learn domain transformation without any fully connected layer. It can effectively reduce the number of parameters when compared with AUTOMAP [12], which makes it possible for large images, offering a powerful tool for solving reconstruction problems in clinically acceptable time.
- Due to the highly computational burden of adjoint, we propose the FI-Net to learn the adjoint from training data rather than computing it directly. Since the computation of FI-Net is much faster than the computation of the adjoint, the training of our proposed network would be hence much faster than the learned PDHG algorithm [13] which needs to compute the adjoint at every unrolled iteration in its network. For the same reason, our trained network would be much faster to use for image reconstruction than the learned PDHG network. Therefore, our network will benefit the community by the various and ubiquitous uses in different reconstruction problems, which need an adjoint as input.

2. Forward model

For conventional iterative image reconstruction, it is necessary to compute the forward model and back - propagation. In USCT, the basis for forward model is the wave propagation of ultrasound which is mathematically described by the wave equation in the frequency domain for inhomogeneous object [1].

2.1. Helmholtz equation

The Helmholtz equation [1] can simulate the ultrasonic wave propagation through a background medium including multiple scattering, and diffraction as

$$\Delta p + k_0^2(1+\eta)^2 p = 0 \tag{2}$$

with the pressure field p. The acoustic medium is described by the background wave number $k_0 = w/c_0$ with the SoS of the background medium c_0 and angular frequency $w = 2\pi f$. The refractive index is $1+\eta$, where $\eta = a + \frac{b}{k_0} i$ is a complex value: its real part $a = \frac{c_0}{c}$ 1 describes the deviation of the SoS (c is in the soft tissue while c_0 is in the background medium), and its imaginary part $\frac{b}{k_0} i$ depends on the parameter b that accounts for the frequency-dependent attenuation.

A full solution of the wave equation is computationally highly demanding since solving the Helmholtz equation is not possible within a reasonable time, which is due to the computation of the used maximal frequencies of up to 3.5 MHz requiring approximately 10 discretization points per wavelength. In practice, an approximation is necessary. A strategy commonly known from geophysics is the paraxial approximation [1,14], which describes the ultrasound field as nearly plane waves in the forward direction.

2.2. Paraxial approximation forward model

For the paraxial approximation [1], we consider that the emitters are put around a circle, while the receivers are on the opposite side of these emitters (see Fig. 2(a)). The wave can propagate from a slice to another slice, and the propagation direction is indicated by z. The forward solution is the frequency dependent pressure field p on the computational grid. The grid is resampled from the reconstruction volume/plane as a set of parallel slices/lines perpendicular to the emission direction (see Fig. 2(b)). The propagation from k^{th} z slice to $(k+1)^{th}$ z slice on the computational grid Nx × Nz with step width Δx and Δz reads

$$p_{k+1} = e^{i\Delta z k_0 \eta_k} * \mathbf{F}^{-1}\left\{ e^{i\Delta z \sqrt{k_0^2 - \xi^2}} * \mathbf{F}(p_k) \right\} \tag{3}$$

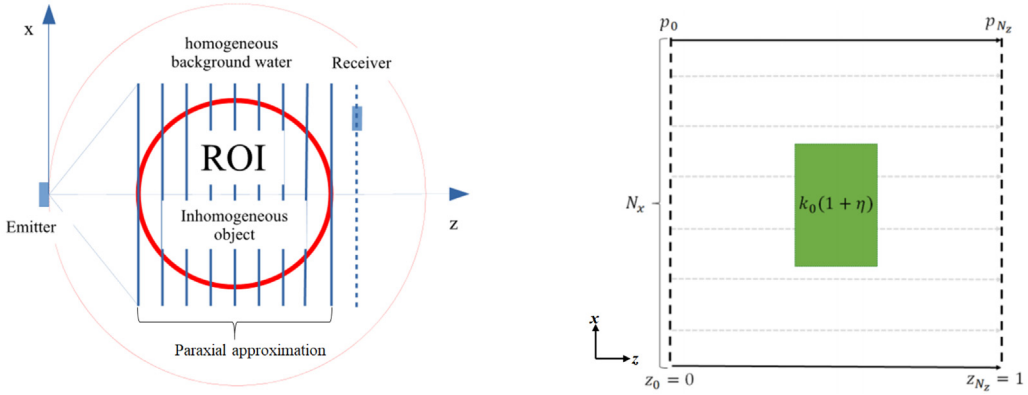

(a) The inhomogeneous object is located in the the region of interest (ROI) indicated by the red circle and covered by the slices of paraxial approximation. The ultrasound is emitted in an approximately spherical wave from the emitter in z-direction.

(b) Measurement set-up: A wave is propagated to determine the breast (green), whereas the homogeneous background (white) is provided by k_0. Based on measurements taken at $z_{Nz} = 1$, the breast can be reconstructed by minimizing the error.

Fig. 2. Forward model and measurement set-up.

where $p = p(x, z)$ with $x, z \in R$ describes the pressure field in 2D in the frequency domain through the propagation direction z; the index k at p and η denotes the k^{th} z slice; the spectral variable reads $\xi = \frac{2\pi}{\Delta x N x}\left[\ \frac{Nx}{2}+1, \ldots, 0, \ldots, \frac{Nx}{2}\right]^T \in \mathrm{R}^{Nx}$; $\mathbf{F}$ and $\mathbf{F}^{-1}$ respectively represent 1D discrete Fourier transformations and the inverse discrete Fourier transformations [15]. Assuming that we have NTE emitters and NT receivers, the full scan includes NTE $\times$ NT waves.

Based on the Eq. (3) of the forward problem, the adjoint of derivative's forward operator is necessary for the back propagation of an iterative scheme. The formula of adjoint is as follow:

$$p_k^* = \mathbf{F}^{\ 1}\left\{e^{\ i\Delta z\sqrt{k_0^2-\xi^2}} * \mathbf{F}(e^{\ i\Delta z k_0 \eta_k} * p_{k+1})\right\} \tag{4}$$

where all parameters have the same meanings as in the Eq. (3).

This is known as an inverse problem, and it is ill-posed due to the nonlinearity and the extremely large scale of the problem. Hence, many iterative reconstruction algorithms are hard to apply due to the computation burden for determining forward operator and its adjoint.

3. Related work

We usually divide existing image reconstruction methods into two categories: model-based methods and data-based methods. In the following section, we will briefly review the two types of methods.

3.1. Model-based reconstruction

In the model-based image reconstruction, the forward and adjoint operators of the imaging problem are directly used in the inverse algorithm [16]. Since the reconstruction η from frequency data p is generally ill-posed, a conventional model-based method for solving problem Eq. (1) is to minimize a regularized objective function by:

$$\eta = \min_{\eta \in X} \mathbf{L}(\mathbf{T}(\eta), p) + \lambda \mathbf{R}(\eta) \tag{5}$$

where the first term is for data consistency and the second term is a regularization prior. Here, λ is regularization parameter. The regularization prior $\mathbf{R}$ is carefully designed to limit the solutions to the space of the desired images, and $\mathbf{L}$ is the negative data log-likelihood.

An iterative model-optimized algorithm called Newton conjugate gradient [1] is proposed to reconstruct USCT images in inhomogeneous media, where it builds the forward model in the pressure field domain and iteratively reconstruct the images. In particular, Valkonen [9] proposes the PDHG algorithm for magnetic resonance imaging (MRI) image reconstruction, which provides a solid basis concerning convergence and theoretical basis for optimization problems. In [17], a total variation (TV) minimization, which uses gradient transformation as regularization prior, obtains some satisfying results in CT reconstruction. Beck and Teboulle [18] develop an iterative shrinkage-thresholding algorithm (ISTA) and Liu et al. [19] present an alternating direction method of multipliers (ADMM) to solve the inverse problems, which are widely used in compressed sensing and MRI reconstruction.

Based on traditional algorithms, model-driven methods in DL introduce forward models and back propagation into neural networks, which use DNNs as regularization prior. Both of ISTA-Net [20] and ADMM-Net [21] map the traditional method into DNNs for compressed sensing reconstruction. Adler and Öktem [16] apply a learned gradient scheme to reconstruct CT images. Kulkarni et al. [22] reduce the computational complexity by weight sharing while training the network. Hammernik et al. [23] propose a learned variational network to unroll the approximate message-passing (AMP) method for inverse problems, which replaces the denoising operator with CNNs.

Model-based reconstruction methods have to repeat the solutions of the forward problem and back propagation. For large, highly non-linear problems like USCT, they suffer from a high computational burden and the management of appropriate regularization strategies and parameters therein. USCT has a highly scattering medium and the waveforms, and it has been used to efficiently determine the curved, non-linear paths of the wave across the refractive media, from source to receivers and back, which makes it more sophisticated than other methods. In a nutshell, USCT cannot neglect wave effects like refraction and diffraction without loosing resolution. So far, most of the USCT breast imaging reconstruction methods are based on an approximation of the acoustic wave equation [24–26]. However, the wave equation or its approximation of the wave equation needs to be solved numer-

ically for a large number of iterations. Hence, the large computational burden makes USCT image reconstruction different from other back-projection based image reconstruction, such as MRI [27], PET [28] and microscopy [29].

3.2. Data-based reconstruction

Another strategy for reconstructing images uses data-driven approaches. These approaches do not require a forward model. They reformulate image reconstruction as a data-driven supervised learning task. They can be split into two categories.

The first category uses DNN as a post-processing method for image reconstruction, artifact removal and denoising. These methods need to learn how to map initial reconstructed low-quality images to high-quality images. For instance, [7,30] use a residual encoder-decoder CNN to generate artifact-free images with FBP reconstructed images as input. Han and Ye [31] use a U-Net as post-processing algorithm for CT image denoising. In [32], a generative adversarial network (GAN) is proposed to clean degraded images.

The second category of data-based image reconstruction methods map the frequency into the image domain by learning the inverse operator from training data. There are fewer methods compared with the post-processing data-based methods. Zhu et al. [12] propose a framework for image reconstruction known as AUTOMAP. The framework improves the reconstruction performance and manifests superior immunity to noise when compared to traditional reconstruction methods. In [33], a deep CED network is proposed to reconstruct PET images directly from PET sinograms.

All mentioned strategies, however, suffer from the huge amount of parameters and necessary training data in order to learn the inverse operator without any system model. Hence, they do not scale well, they cannot be applied to large images and the overall performance is limited.

4. Methodology

In order to combine the advantageous properties of model-based and data-based methods and to overcome their limitations, we propose a hybrid model-data-driven image reconstruction approach. The goal is to design a deep neural network architecture that directly and quickly reconstructs high-quality images from USCT data without computation of adjoints. To the best of our knowledge, this is also the first work in the field of USCT image reconstruction based on DL.

4.1. Preliminaries

Iterative unrolled network is based on unrolling conventional iterative algorithms and using CNNs to replace the penalty functions. Our network is based on the PDHG algorithm, which is a typical iterative reconstruction method and a first order proximal method [9]. Due to its robustness, it is well suited for solving a large class of inverse problems, and it has been successively applied in different fields [13,34]. It solves the underlying optimization problem simultaneously with its dual, which provides a robust convergence check. Specifically, PDHG (Algorithm 1) solves the problem in Eq. (5) by iterating between the following update steps:

$$p^{(n+1)} = \text{prox}_{\sigma L^*}\left(p^{(n)} + \sigma \mathbf{T}(\eta^{(n)})\right) \tag{6}$$

where $p \in \mathbf{Y}, \eta \in \mathbf{X}, n$ denotes the PDHG iteration index, $p^{(n+1)}$ is optimization result at the $(n+1)^{th}$ iteration, $\mathbf{L}^*$ is the convex conjugate of $\mathbf{L}$, and σ is step size. This update step is in the dual space.

For the update step in the primal space, it reads:

$$\begin{aligned} \eta^{(n+1)} &= \text{prox}_{\tau R}\left(\eta^{(n)} - \tau\left[\partial \mathbf{T}(\eta^{(n)})\right]^*(p^{(n+1)})\right) \\ \bar{\eta}^{(n+1)} &= \eta^{(n+1)} + \gamma(\eta^{(n+1)} - \eta^{(n)}) \end{aligned} \tag{7}$$

Here, $\left[\partial \mathbf{T}(\eta^{(n)})\right]^* : \mathbf{Y} \to \mathbf{X}$ is the adjoint of the derivative of $\mathbf{T}$ regarding η, and τ is step size. γ is overrelaxation parameter and **prox** is the proximal operator. Formally, the proximal operator is defined as

$$\text{prox}_{\lambda \mathbf{R}}(\eta) = \arg\min_{\eta' \in X}\left(\mathbf{R}(\eta) + \frac{1}{2\lambda}||\eta' - \eta||_2^2\right) \tag{8}$$

Algorithm 1. Primal dual hybrid gradient (PDHG)

1: **Given:** $\sigma, \tau, N > 0, \gamma \in [0,1]$ and $p_0 \in \mathbf{Y}, \eta_0 \in \mathbf{X}$
2: **for** $n = 1, \ldots, N$ **do**
3: $\quad p^{(n+1)} = \text{prox}_{\sigma L^*}\left(p^{(n)} + \sigma \mathbf{T}(\eta^{(n)})\right)$
4: $\quad \eta^{(n+1)} = \text{prox}_{\tau R}\left(\eta^{(n)} \quad \tau\left[\partial \mathbf{T}(\eta^{(n)})\right]^*(p^{(n+1)})\right)$
5: $\quad \eta^{(n+1)} = \eta^{(n+1)} + \gamma(\eta^{(n+1)} \quad \eta^{(n)})$
6: **end for**

Due to the success of DL, the iterative unrolled network of learned PDHG [13] that combines DL with model-based reconstruction is proposed to solve inverse problems. It unrolls the proximal primal-dual method, and replaces proximal operators with CNNs. A learnable DNN (Algorithm 2) replaces the proximal operator in Eq. (6):

$$p^{(n+1)} = f_R\left\{p^{(n)} + \sigma^{(n+1)} \mathbf{T}(\eta^{(n)}); \mathbf{\Theta}^{(n+1)}\right\} \tag{9}$$

where $f_R(p; \Theta)$ is the neural network with pressure field p and parameter Θ as inputs. The parameters of Θ and σ can be learned during the training progress:

$$\sigma^{*(1)}, \mathbf{\Theta}^{*(1)}, \ldots, \sigma^{*(N)}, \mathbf{\Theta}^{*(N)} = \arg\min_{\sigma^{(1)}, \mathbf{\Theta}^{(1)}, \ldots, \sigma^{(N)}, \mathbf{\Theta}^{(N)}} \sum_i ||p_i^{(N)} - p_i^{true}||_2^2$$

where $p_i^{(N)}$ and p_i^{true} are the i^{th} generated pressure filed and the corresponding reference pressure filed.

For the primal space, the unrolled network of Eq. (7) reads:

$$\begin{aligned} \eta^{(n+1)} &= f_R\left\{\eta^{(n)} - \tau^{(n+1)}\left[\partial \mathbf{T}(\eta^{(n)})\right]^*(p^{(n+1)}); \mathbf{\Lambda}^{(n+1)}\right\}, n \\ &= 1, 2, \ldots, N \end{aligned} \tag{10}$$

where $f_R(\eta; \mathbf{\Lambda})$ is a CNN, and the parameters $\mathbf{\Lambda}, \tau$ can be learned from:

$$\tau^{*(1)}, \mathbf{\Lambda}^{*(1)}, \ldots, \tau^{*(N)}, \mathbf{\Lambda}^{*(N)} = \arg\min_{\tau^{(1)}, \mathbf{\Lambda}^{(1)}, \ldots, \tau^{(N)}, \mathbf{\Lambda}^{(N)}} \sum_i ||\eta_i^{(N)} - \eta_i^{true}||_2^2$$

where $\eta_i^{(N)}$ and η_i^{true} are the i^{th} image reconstruction result and the corresponding ground truth;

For this kind of iterative unrolled network, the computation time of forward model $\mathbf{T}$ and the adjoint of derivative's forward operator $\left[\partial \mathbf{T}(\eta^{(n)})\right]^* : \mathbf{Y} \to \mathbf{X}$ is dominating, and as a result, it fails to reduce the overall computation time significantly.

Algorithm 2. Learned PDHG

1: **Given:** $p_0 \in \mathbf{Y}, \eta_0 \in \mathbf{X}$
2: **for** $n = 1, \ldots, N$ **do**
3: $\quad p^{(n+1)} = f_R\left\{p^{(n)} + \sigma^{(n+1)} \mathbf{T}(\eta^{(n)}); \mathbf{\Theta}^{(n+1)}\right\}$
4: $\quad \eta^{(n+1)} = f_R\left\{\eta^{(n)} \quad \tau^{(n+1)}\left[\partial \mathbf{T}(\eta^{(n)})\right]^*(p^{(n+1)}); \mathbf{\Lambda}^{(n+1)}\right\}$
5: $\quad \eta^{(n+1)} = \eta^{(n+1)} + \gamma(\eta^{(n+1)} \quad \eta^{(n)})$
6: **end for**

4.2. Network architecture

In order to solve highly non-linear inverse problems in relatively short time, we propose a dual domain network architecture for USCT reconstruction based on learned PDHG [13] as described in Algorithm 2. Both learned PDHG [13] and our algorithm unroll the PDHG algorithm, and replace proximal operators with CNNs. But differently, we use the FI-Net to replace the computation of $[\partial \mathbf{T}(\eta^{(n)})]^*$ in the primal space to save computation time.

The proposed neural network architecture involves CNNs in both the frequency space and image space. As shown in Fig. 3, our proposed model consists of two parts: (a) In the dual space, we perform an optimization of the data term. Our algorithm generates the frequency data according to the forward model and then we optimize the data according to the realistic data. (b) In the primal space, a FI-Net reconstructs the images according to the output of the dual space to transform frequency domain to image domain. The detailed description of the functionality and network design of the dual space and primal space is given in Subsections 4.2.1 and 4.2.2, respectively.

Inputs to the network just need pressure field data $p \in \mathbf{Y}$. During iteration, the points p_0 and η_0 in the dual and primal space are initialized by zero in the beginning. Let the number of unrolled iterations be N = 3 because of memory problem. In the dual space, we first apply the forward model to generate an initial estimate of the frequency data. Then, we use CNNs to allow the network to minimize the data. Finally, according to the output of the dual space, the reconstructed USCT image $\eta_n \in \mathbf{X}$ is reconstructed by the FI-Net.

4.2.1. Deep neural network in dual space

By taking full advantage of the properties of both, PDHG and network-based methods, the basic idea of our architecture is to map the previous PDHG update steps into a deep network architecture that consists of a fixed number of iterations, each of which corresponds to one iteration in the traditional PDHG.

At the top of Fig. 3, an optimization of the data term is performed in the dual space. At first, we need to concatenate the initial guess dual variable p_n, frequency data p and the output of

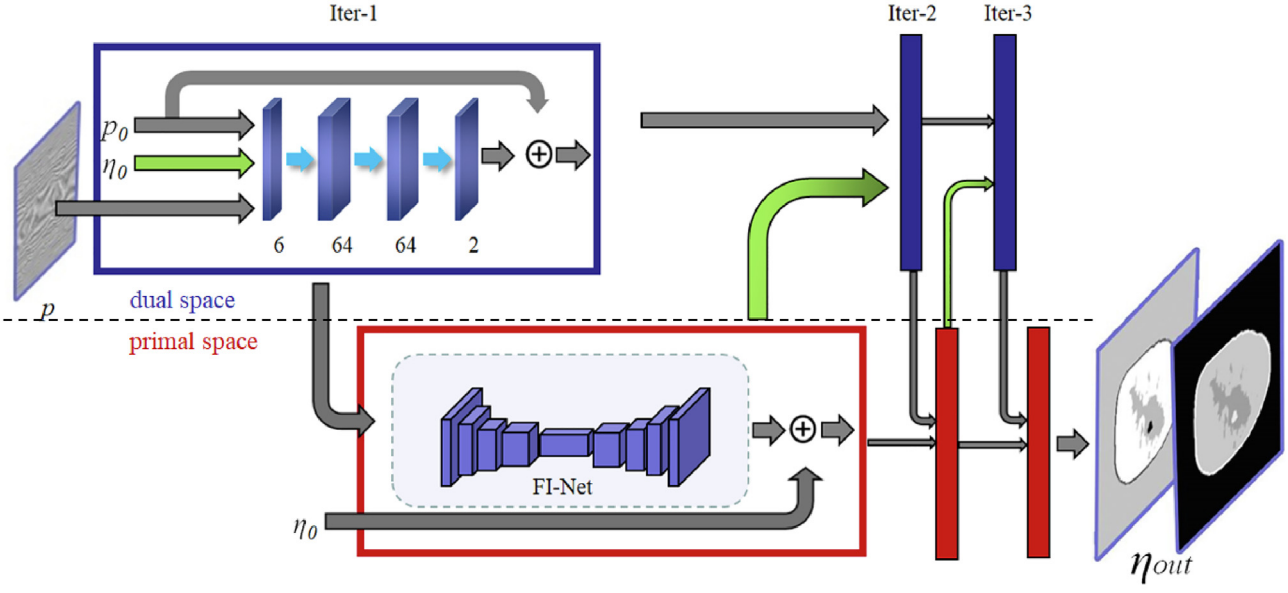

(a) The whole architecture of proposed network

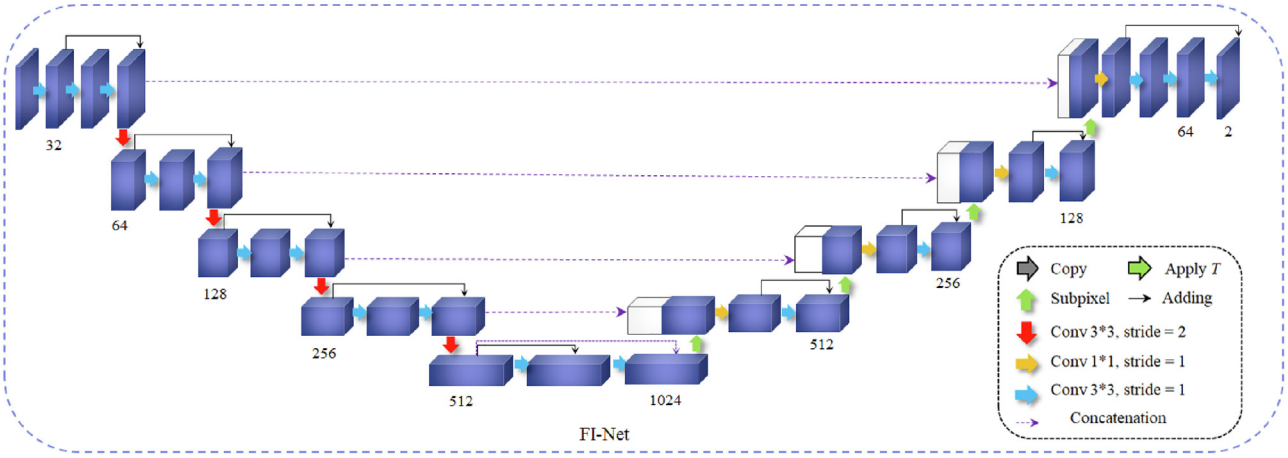

(b) Structure of FI-Net

Fig. 3. The proposed network architecture for USCT reconstruction. In (a), the dual iterations are in blue boxes, while the primal iterations are in red boxes. The blue/red boxes all have the same architecture during the iteration, which is illustrated in the corresponding large boxes. The connection pointing to one box indicates concatenation.

$\mathbf{T}(\eta_n)$. Neural networks optimize the dual variable p instead of the primal proximal according to Eq. (6).

The part of dual space consists of a 3-layer network, where the convolutions in the dual space are all 3×3 pixels in size with stride 1, and the number of channels is 6-64-64-2, followed by a rectified linear unit (ReLU). In USCT, we operate with complex numbers, hence, we stack the real (SoS) and imagery (attenuation) parts as two channels, where the 6 channels of inputs are 2×3 $(p_0, p, \mathbf{T}(\eta))$, while the 2 channels of the reconstructed output represent SoS and attenuation.

4.2.2. FI-Net

For most model-optimized iterative algorithms [8,9,35,20,36], an adjoint of the derivative of $\mathbf{T}$ in the PDHG and learned primal-dual is required as input. Computing the adjoint of the derivative of forward model is relatively complex and is very time consuming. In order to overcome this expensive computation of the adjoint, our FI-Net Ψ computes the adjoint of the derivative of $\mathbf{T}$ by CNNs:

$$\eta^{(n+1)} = f_R\{\eta^{(n)} + \psi^{(n)}(p^{(n+1)})\}, \ n = 1, 2, \ldots, N \tag{11}$$

where p_n is the output of the dual space.

The network architecture of the FI-Net is depicted in the bottom part of Fig. 3(b). The network consists of two parts. The first part consists of sequential blocks of 3×3 convolutions with stride 2 to realize down-sampling, where the number of channels in the different layers is $32 \rightarrow 64 \rightarrow 128 \rightarrow 256 \rightarrow 512$, with a twofold increase in the number of channels, and followed by a rectified linear unit (ReLU). The first part output consists of 512 feature maps. The second part upsamples the feature maps from the output of the first part. The parameters are mentioned in FI-Net of Fig. 3(b).

Unlike U-Net that uses a 2×2 deconvolution layer to upsample the feature maps, our upsampling block includes 2 layers: a 3×3 convolution layer and a sub-pixel convolutional layer [37,38] since the sub-pixel layer could expand the feature maps efficiently. The subpixel layer allows the neural network to propagate more detailed information directly from lower space to higher space instead of zero padding and interpolation, which helps enhance the accuracy at pixel level.

5. Experiments

5.1. Experimental design

We evaluate the algorithm on USCT problems with different methods. All the compared approaches are evaluated on the same Optical and Acoustic Breast Phantom Database (OA-Breast dataset), described below in more detail.

5.1.1. OA-Breast dataset

Lou et al. [39] published a 3D optical and acoustic breast phantom dataset for various acoustic imaging simulation and optical studies. The OA-Breast dataset provides for three patients MRI-data with different breast density levels: extremely dense, heterogeneously dense and scattered fibroglandular level. The 3D rendered views are shown in Fig. 4. Each of the 3D data sets contains many 2D slices, where the different tissue pixel is labeled as different integer in the 2D slices (see Table 1).

For the extracted 2D slices from 3D data, we need to assign η according to the parameters in Table 1 for different tissues [1,15]. And then a Gaussian filter is applied on η to ensure each tissue has a smooth gradient [15]. The data is then processed by the paraxial approximation forward model of Eq. (4) according to the value of η. Random Gaussian noise is applied on the data to augment data. Specially, considering the accuracy of reconstruction and convergence, the range of Signal to Noise Ratio (SNR) is set as 110 to 140 dB. Finally, the data is scaled to the range of (0, 1) to generate the simulated USCT dataset for training, validation and test.

4,000 2D slices are extracted from OA-Breast dataset. Specifically, 2,000 images are used as training set. These training images are further quadrupled by data augmentation: 90 degree rotation, grayscale-value reversing and 90 degree rotation of generated images. After data augmentation, the total 2000×4 images are used for training. 1,000 images from OA-Breast dataset are used for the validation set and the rest 1,000 images are used for test. All these three sets are kept separate.

For the generated USCT dataset, the size of frequency data is 256×128 at the start frequency of 0.5 MHz, and the size of outputs is 256×256 with pixel size 1.88 mm. The radius of ROI is 80 mm and the radius of USCT device is 130 mm.

5.1.2. Implementation details

The model was implemented in TensorFlow framework [40] and trained with one GTX 1080Ti GPU card. The following mean absolute error (MAE) loss serves as loss function,

$$MAE = \frac{1}{n}\left(\sum_{i=1}^{n}|\hat{\eta}_{sos} - \eta_{sos}| + \sum_{i=1}^{n}|\hat{\eta}_{att} - \eta_{att}|\right) \tag{12}$$

where η_{sos} and η_{att} are the ground truth of SoS and attenuation; $\hat{\eta}_{sos}$ and $\hat{\eta}_{att}$ are the reconstructed images of SoS and attention.

Xavier initialization scheme [41], ADAM optimizer [42] with parameters $(\beta 1, \beta 2) = (0.5, 0.99)$ and batch size of 16 are used for model training. The learning rate in step t is:

$$l_t = \frac{l_0}{2}\left(1 + \cos(\pi \frac{t}{t_{\max}})\right) \tag{13}$$

with $l_0 = 10^{-4}$. The model is optimized on the training set over 280 epochs.

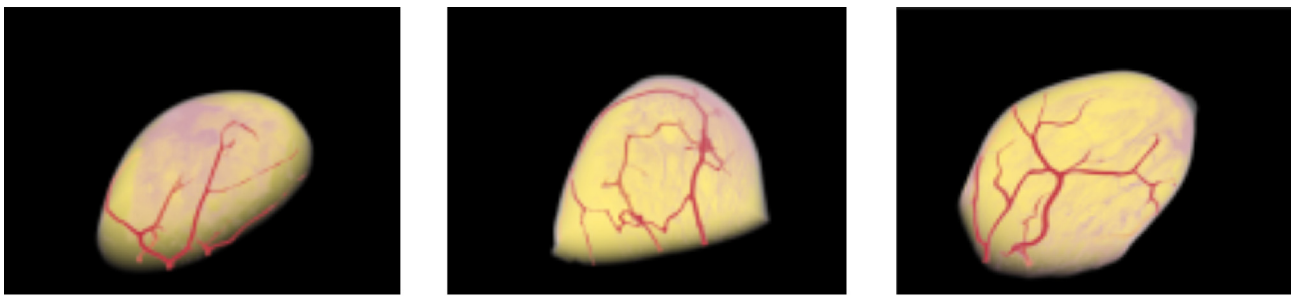

(a) extremely dense breast (b) heterogeneously dense breast (c) scattered fibroglandular breast

Fig. 4. 3D rendered views of OA-Breast dataset.

Table 1
The parameters for USCT breast data.

Type of issue in OA-breast	Speed of sound (SoS)	Attenuation in dB/m/MHz
0: background(water)	1485 m/s	0
2: fibro-glandular tissue	1490 m/s	0.88
3: fat	1450 m/s	1.26
4: skin layer	1570 m/s	2.08
5: blood vessel	1560 m/s	1.60

5.2. Experimental results

In order to show the performance of our algorithm, we compare our model with the following methods: 1) PDHG [9], 2) Newton Conjugate Gradient (CG)[11], 3) U-Net [43], 4) FC-DenseNet103 [44], and 5) Densely Connected Hierarchical Network (DHDN) [45] on test set. The first two are traditional iterative optimized methods and the rest are DL methods. Here, we exclude the experiments of learned PDHG [13], since it needs to compute the adjoint at every unrolled iteration in its network. In our USCT application, the adjoint is very expensive to compute. As a result, training the learned PDHG network would be extremely slow. We failed to train it within realistic time to get meaningful results.

Quantitative Comparisons. The root mean squared error (RMSE) and structural similarity measure (SSIM) are the evaluation metrics for quantitative evaluations. Table 2 shows quantitative comparisons with different noise levels on the test set. We separate quantitative comparison to three comparison levels: traditional iterative optimized methods and DL methods level, SoS and attenuation level, and noisy data with noise free level.

Table 2
Quantitative evaluation of results on test set in terms of SSIM and RMSE with different noise levels.

SSIM/RMSE	SoS (real part)			Attenuation (imaginary part)		
	SNR = 30	SNR = 50	Noise free	SNR = 30	SNR = 50	Noise free
1) PDHG	0.532/0.208	0.756/0.143	0.966/0.009	0.479/0.335	0.480/0.335	0.481/0.335
2) Newton CG	0.546/0.198	0.747/0.143	**0.971/0.009**	0.480/0.335	0.473/0.336	0.481/0.335
3) U-Net	0.732/0.145	0.736/0.144	0.737/0.144	0.708/0.173	0.714/0.171	0.714/0.171
4) FCdense103	0.720/0.145	0.720/0.145	0.739/0.139	0.693/0.173	0.696/0.172	0.719/0.164
5) DHDN	0.705/0.145	0.704/0.144	0.724/0.141	0.621/0.173	0.620/0.173	0.686/0.168
6) Ours	**0.952/0.096**	**0.955/0.095**	0.956/0.095	**0.943/0.109**	**0.944/0.109**	**0.945/0.109**

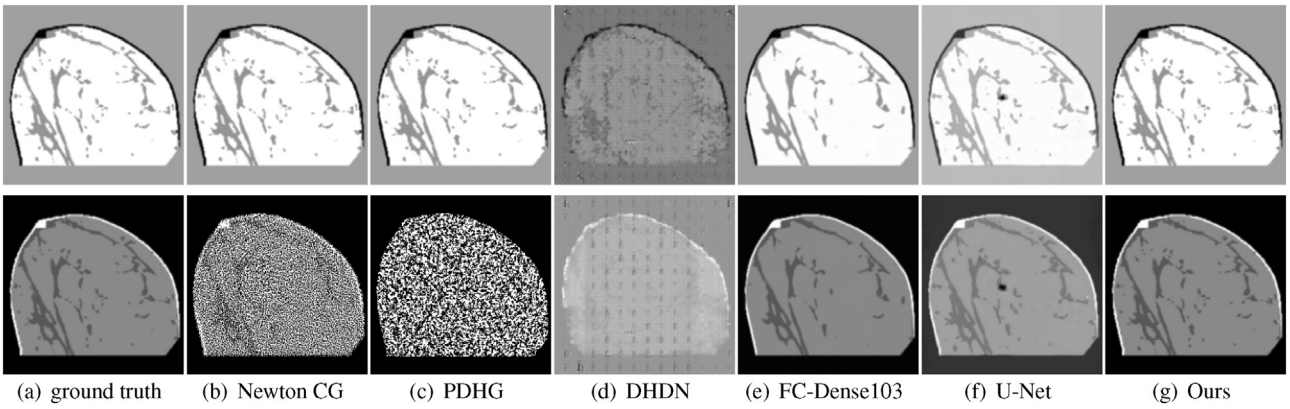

Fig. 5. Visual comparisons on USCT for different algorithms without noise, the first row shows the SoS reconstructed results, while the second row shows the attenuation.

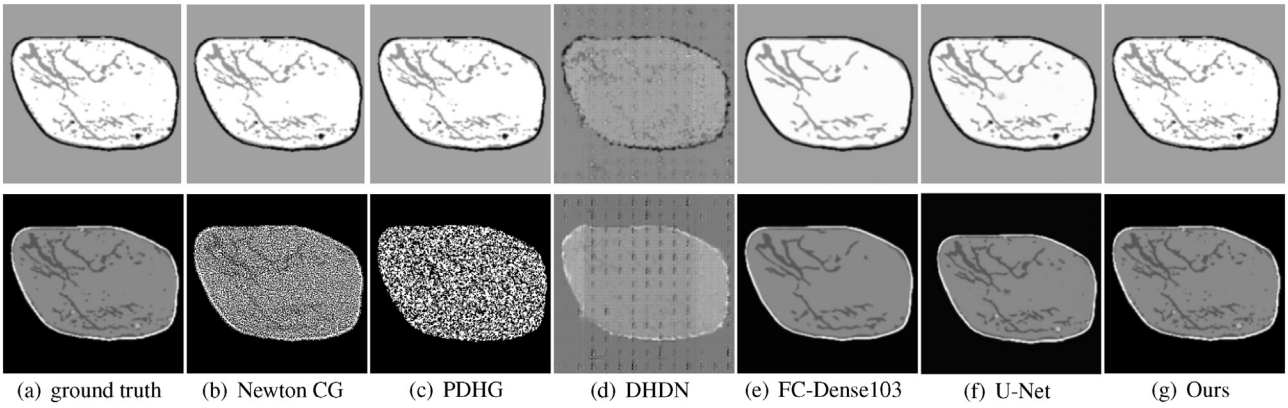

Fig. 6. Visual comparisons on USCT for different algorithms with SNR = 50 dB.

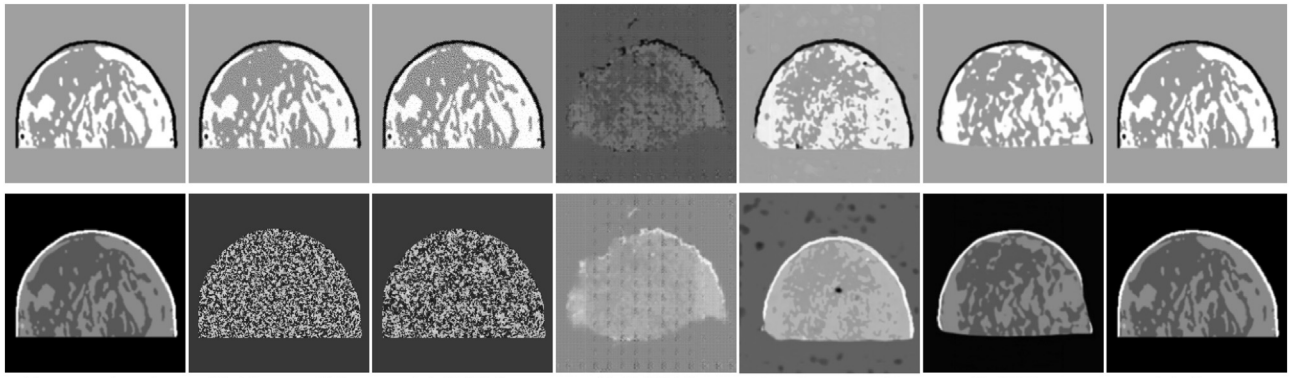

(a) ground truth (b) Newton CG (c) PDHG (d) DHDN (e) FC-Dense103 (f) U-Net (g) Ours

Fig. 7. Visual comparisons on USCT for different algorithms with SNR = 30 dB.

Comparing traditional iterative optimized methods with DL methods, we find that the initialization of Newton CG and PDHG should be chosen carefully in order to get better results. In the paper, for Newton CG and PDHG, we use mean value of ROI as the initialization. In our method we use zero-initialization, because DL does not have this high sensitivity for the attenuation. For the noise-free case in SoS, Newton CG and PDHG achieve similar results and better reconstructed results when compared with DL techniques, since both of the forward model and back propagation are solved numerically for a great number of times during each iteration. But for the rest of the cases, DL methods obtain better results than the iterative optimized methods. However, we observe that the DL approaches U-Net, FC-DenseNet103 and DHDN cannot reconstruct images well on all levels when compared with our algorithm. The reason is that the network needs to learn the transform from the frequency to image domain and it is non-linear and complex, see the forward model and adjoint in Eqs. (3), (4). These DL network architectures don't have high performance on USCT images.

For the SoS and attenuation comparison, all of the algorithms achieve better reconstructed SoS images than their own attenuation images since attenuation is much smaller than SoS and it starts to converge only after the SoS is well reconstructed. For the attenuation, however, only our proposed algorithm can achieve

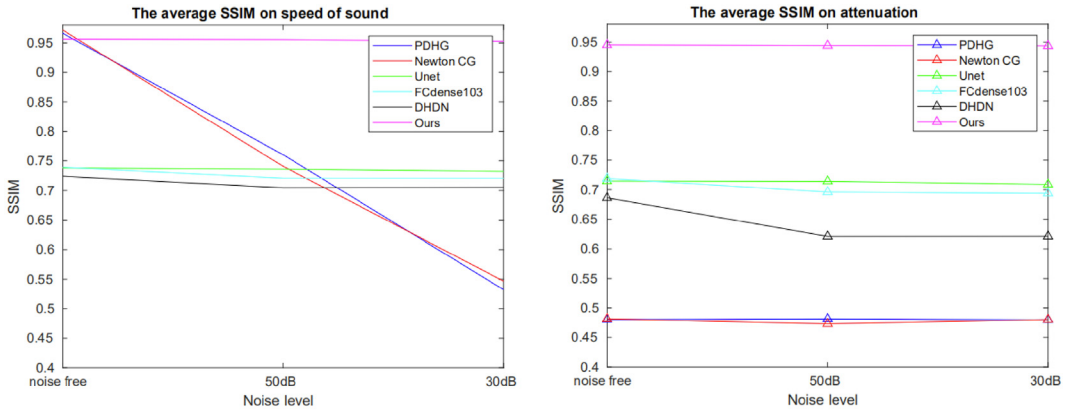

(a) SSIM results on SoS

(b) SSIM results on attenuation

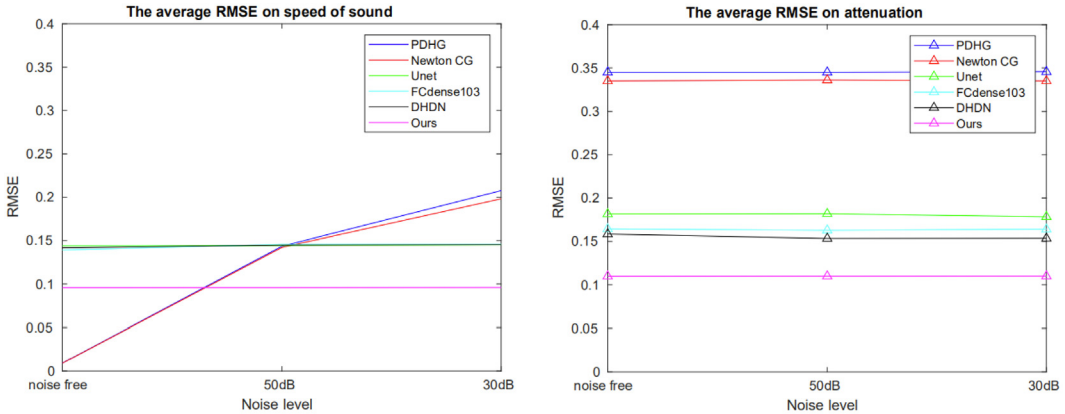

(c) RMSE results on SoS

(d) RMSE results on attenuation

Fig. 8. Quantitative evaluation on USCT images. Different colored lines indicate different reconstruction algorithms. The lines with a triangle indicate the quantitative results of attenuation, while the left lines are the SoS results.

acceptable results with 0.944 SSIM and 0.109 for RMSE. For most cases in the SoS part, our method also achieves significant improvements over other methods.

As for noisy data, DL methods clearly outperform Newton CG and PDHG due to the ability to substantially denoise the images while inverting the problem. For DHDN, it achieves lower accuracy when compared with U-Net and FCdense103. It uses a modified U-Net hierarchical architecture to enable the network to use a large number of parameters, but it adds the final output to the initial input, which makes hard reconstruct images from frequency domain to image domain. However, the Newton CG and PDHG can compute the adjoint of derivative of forward model, and they can achieve higher SSIM than U-net, FC-DenseNet103 and DHDN without noisy data for the SoS part. When compared with other methods on all the three levels, our method improves the SSIM from 0.690 to 0.954 and RMSE from 0.156 to 0.095 on average concerning the SoS reconstruction, while it improves the SSIM from 0.596 to 0.943 and RMSE from 0.238 to 0.109 on average in attenuation reconstruction.

Visual Comparisons. Figs. 5–7 show visual results of USCT 2D slices at different noise levels in test set. The first row of Figs. 5–7 shows the reconstruction results of SoS with noise free, SNR 50 dB, SNR 30 dB respectively, while the second row of Figs. 5–7 shows the corresponding results of attenuation. And the plots of SSIM and RMSE values are shown in Fig. 8. We note that small structures, such as the small inserts and dots, are much more clearly visible in our method than the other methods. For Newton CG and PDHG, both of them can reconstruct the SoS well without noise. But for the attenuation and noisy data, even though both of Newton CG and PDHG have good initialization, it is difficult for them to reconstruct attenuation while our method achieves a good quality. For the DL methods U-Net, FC-DenseNet103 and DHDN, none of them can reconstruct more detailed information. Our method attains the best performance in terms of both SSIM and RMSE consistently in most categories.

In addition, we report our USCT reconstruction results with more detailed information (see Fig. 9). The starting frequency is 0.5 MHz and it reaches the final frequency 2.5 MHz. In Fig. 9, the 2D images of Fig. 9(a) and (b) are reconstructed SoS and attenuation respectively. The 1D profiles of Fig. 9(c) and (d) focus on the parameters/pixels at the pink dotted lines, where the reconstructed profiles are given in red and their simulated reference in blue. In Fig. 10, we give more visual results to show robustness.

Running Time Comparisons. On one Nvidia 1080Ti GPU card, it takes 1.31s for our method to reconstruct SoS and attenuation from pressure field. For the DL methods, U-Net, FC-DenseNet103 and DHDN needs 0.087s, 0.136s and 0.162s respectively. As shown in Fig. 11, Newton CG and PDHG cost about 66 minutes to reconstruct one high-quality image due to the need for repeated iterative operations, while other DL methods have relatively lower reconstruction quality. The DL based methods run faster than the traditional image reconstruction methods. Because these learned methods belong to data-driven methods, they are much faster without forward solution. The reason for the speedup is, once the partial inverse is learned, only a forward pass through the network is necessary without the need to perform a forward solution of the ultrasound transport model; this saves a lot of computing time.

6. Discussion

The main focus of this paper is to introduce a model- and data-driven framework for USCT reconstruction and demonstrate its benefits when compared with traditional methods. Furthermore, our framework does not rely on any initial reconstruction as input: it can reconstruct images directly from frequency domain to image domain.

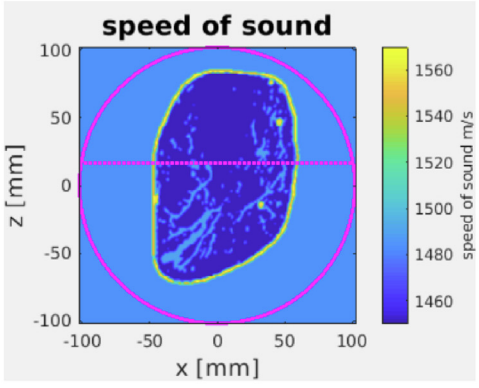

(a) SoS reconstruction result

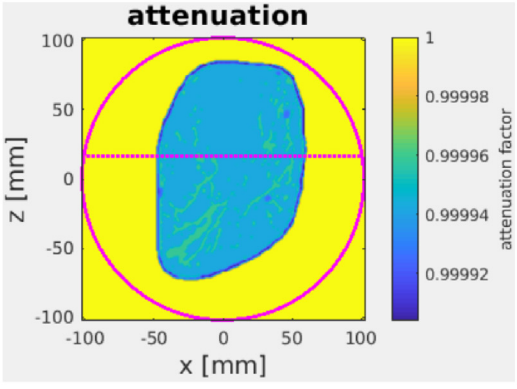

(b) Attenuation result

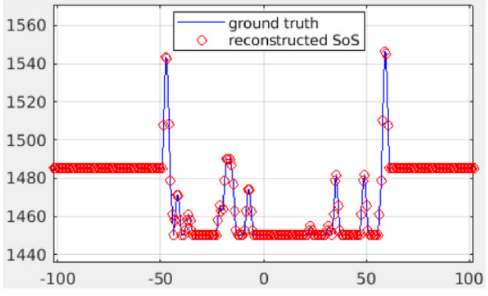

(c) SoS 1D profiles

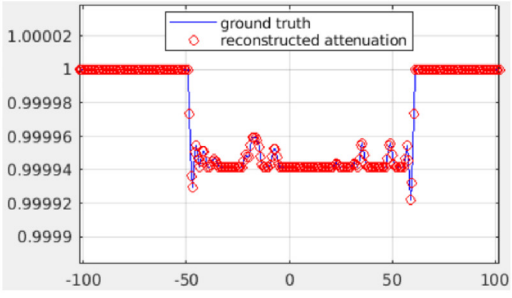

(d) Attenuation 1D profiles

Fig. 9. Visual reconstruction result and its 1D profiles focusing on the pixels at the pink dotted line where the reconstructed profiles are given in red circles and their simulated reference in blue.

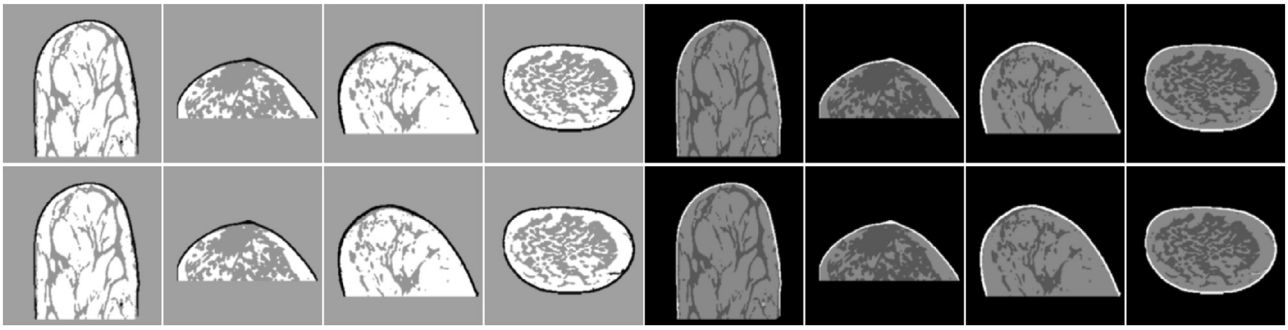

Fig. 10. Visual results of more phantoms. The top results are the ground truth images while the bottom results are the reconstructed results. The left four columns are SoS results while the right four columns are attenuation results.

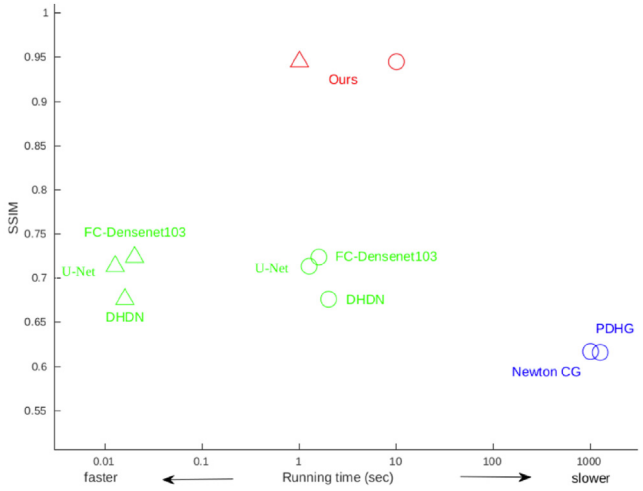

Fig. 11. The reconstruction quality and running speed comparison. ○ and △ present the CPU implementation time and the GPU implementation time, respectively. The compared traditional methods are marked with blue font; the compared deep learning methods are marked with green font; our method is marked with red color.

Compared with the state-of-the-art reconstruction methods, in particular for noisy data, our algorithm outperforms classical reconstruction algorithms by large SSIM and small RMSE. Compared with PDHG and Newton CG, it can increase SSIM by up to 30% and reduce RMSE by up to 60% for the SoS reconstruction, and increase SSIM by up to 100% and reduce RMSE by up to 70% for attenuation reconstruction. The first reason for good performance for noisy data is that our algorithm learns a regularized partial inverse of the problem whereby the regularization is structure dependent. It determines a regularization functional that allows to compensate noise without substantial loss of image details. Another reason for good performance is that we add different noise levels in the training data, improving the reconstruction with the noise data.

However, because the network uses forward operator, it needs to apply different forward operators in different reconstruction problems. Besides it, we generally do not have a guarantee of achieving a global solution, i.e to be near to the reference solution. Although empirical evidence shows that the method is quite robust, there is still the open problem of guarantees to be solved. On the other hand, DL techniques, again, have demonstrated to be able to capture internal structure information of a problem and learn the partial inverse, offering a new tool for solving difficult reconstruction problems in relatively short time. In addition, we still have the option to verify the quality of the reconstruction by the data term of conventional techniques although it must be said that the regularization is still a black box in this inversion process. Better insights in the internal mapping of the network might help better understand this issue.

All in all, our algorithm is allowed to achieve reasonable reconstruction time for clinical systems with moderate hardware effort and this is also the first work in the field of USCT image reconstruction based on DL. Henceforth, we consider this technique to become a dominant strategy for this and many other inverse problem solving techniques.

7. Conclusion

In this paper, we present a model-data-driven image reconstruction method for USCT images. The algorithm is inspired by the PDHG algorithm, where we use FI-Net in the primal space in order to reduce the time for computing adjoint of derivative of forward operator. The algorithm is neither a typical model-driven method nor a purely data-driven method: it incorporates these two frameworks. Although it requires to apply different forward operators in different applications, and we generally do not have a guarantee of achieving a global solution, it can still be used to solve the inverse problem in USCT and get a good result compared with other typical methods. Future work will be focused on extending this algorithm to realistic size 3D USCT data.

CRediT authorship contribution statement

Yuling Fan: Conceptualization, Methodology, Software, Validation, Writing - original draft, Visualization. **Hongjian Wang:** Conceptualization, Methodology, Formal analysis, Supervision, Writing - review & editing. **Hartmut Gemmeke:** Resources, Investigation, Data curation. **Torsten Hopp:** Resources, Investigation, Data curation. **Juergen Hesser:** Supervision, Writing - review & editing.

Declaration of Competing Interest

The authors declare that they have no known competing financial interests or personal relationships that could have appeared to influence the work reported in this paper.

Acknowledgment

This work was supported by “the Fundamental Research Funds for the Central Universities” from Donghua University under grants No. 2232020D-36, the Donghua University Initial Research Funds for Young Teachers under grants No.112-07-0053079, the Deutsche Forschungsgemeinschaft (DFG) under grants No. HE

3011/37-1 and HO 5565/2-1. The authors acknowledge the authors of [13], Washington University in St. Louis for the source data and the models.

References

[1] H. Gemmeke, L. Althaus, K.W. Van Dongen, H. Egger, J. Hesser, J. Mayer, N.V. Ruiter, M. Zapf, T. Hopp, Wave equation based transmission tomography, in: 2016 IEEE International Ultrasonics Symposium (IUS), 2016, pp. 1–4.

[2] B. Ranger, P.J. Littrup, N. Duric, P. Chandiwala-Mody, C. Li, S. Schmidt, J. Lupinacci, Breast ultrasound tomography versus MRI for clinical display of anatomy and tumor rendering: preliminary results, American Journal of Roentgenology 198 (1) (2012) 233–239.

[3] J.F. Greenleaf, R.C. Bahn, Clinical imaging with transmissive ultrasonic computerized tomography, IEEE Transactions on Biomedical Engineering (2) (1981) 177–185.

[4] H. Chen, Y. Zhang, Y. Chen, J. Zhang, W. Zhang, H. Sun, Y. Lv, P. Liao, J. Zhou, G. Wang, LEARN: Learned experts assessment-based reconstruction network for sparse-data CT, IEEE Transactions on Medical Imaging 37 (6) (2018) 1333–1347.

[5] Y.S. Han, J. Yoo, J.C. Ye, Deep residual learning for compressed sensing CT reconstruction via persistent homology analysis, arXiv preprint arXiv:1611.06391..

[6] K.H. Jin, M.T. McCann, E. Froustey, M. Unser, Deep convolutional neural network for inverse problems in imaging, IEEE Transactions on Image Processing 26 (9) (2017) 4509–4522.

[7] Z. Zhang, X. Liang, X. Dong, Y. Xie, G. Cao, A sparse-view ct reconstruction method based on combination of densenet and deconvolution, IEEE Transactions on Medical Imaging 37 (6) (2018) 1407–1417.

[8] A. Chambolle, T. Pock, A first-order primal-dual algorithm for convex problems with applications to imaging, Journal of Mathematical Imaging and Vision 40 (1) (2011) 120–145.

[9] T. Valkonen, A primal–dual hybrid gradient method for nonlinear operators with applications to MRI, Inverse Problems 30 (5) (2014) 055012.

[10] E.Y. Sidky, J.H. Jørgensen, X. Pan, Convex optimization problem prototyping for image reconstruction in computed tomography with the Chambolle-Pock algorithm, Physics in Medicine & Biology 57 (10) (2012) 3065.

[11] H. Gemmeke, N. Ruiter, 3D ultrasound computer tomography for medical imaging, Nuclear Instruments and Methods in Physics Research Section A: Accelerators, Spectrometers, Detectors and Associated Equipment 580 (2) (2007) 1057–1065.

[12] B. Zhu, J.Z. Liu, S.F. Cauley, B.R. Rosen, M.S. Rosen, Image reconstruction by domain-transform manifold learning, Nature 555 (7697) (2018) 487–492.

[13] J. Adler, O. Öktem, Learned primal-dual reconstruction, IEEE Transactions on Medical Imaging 37 (6) (2018) 1322–1332.

[14] H. Wang, H. Gemmeke, T. Hopp, J. Hesser, Accelerating image reconstruction in ultrasound transmission tomography using L-BFGS algorithm, Medical Imaging 2019: Ultrasonic Imaging and Tomography, vol. 10955, International Society for Optics and Photonics, 2019, 109550B.

[15] W. Zhao, H. Wang, H. Gemmeke, K.W. van Dongen, T. Hopp, J.W. Hesser, Ultrasound transmission tomography image reconstruction with fully convolutional neural network, Physics in Medicine & Biology..

[16] J. Adler, O. Öktem, Solving ill-posed inverse problems using iterative deep neural networks, Inverse Problems 33 (12) (2017) 124007.

[17] E.Y. Sidky, X. Pan, Image reconstruction in circular cone-beam computed tomography by constrained, total-variation minimization, Physics in Medicine & Biology 53 (17) (2008) 4777.

[18] A. Beck, M. Teboulle, A fast iterative shrinkage-thresholding algorithm for linear inverse problems, SIAM Journal on Imaging Sciences 2 (1) (2009) 183–202.

[19] H. Liu, B. Song, H. Qin, Z. Qiu, An adaptive-ADMM algorithm with support and signal value detection for compressed sensing, IEEE Signal Processing Letters 20 (4) (2013) 315–318.

[20] J. Zhang, B. Ghanem, ISTA-Net: Interpretable optimization-inspired deep network for image compressive sensing, in: Proceedings of the IEEE Conference on Computer Vision and Pattern Recognition, 2018, pp. 1828–1837.

[21] Y. Yang, J. Sun, H. Li, Z. Xu, ADMM-Net: A deep learning approach for compressive sensing MRI, arXiv preprint arXiv:1705.06869..

[22] K. Kulkarni, S. Lohit, P. Turaga, R. Kerviche, A. Ashok, Reconnet: Non-iterative reconstruction of images from compressively sensed measurements, in: Proceedings of the IEEE Conference on Computer Vision and Pattern Recognition, 2016, pp. 449–458.

[23] K. Hammernik, T. Klatzer, E. Kobler, M.P. Recht, D.K. Sodickson, T. Pock, F. Knoll, Learning a variational network for reconstruction of accelerated MRI data, Magnetic Resonance in Medicine 79 (6) (2018) 3055–3071.

[24] P. Huthwaite, F. Simonetti, High-resolution imaging without iteration: A fast and robust method for breast ultrasound tomography, The Journal of the Acoustical Society of America 130 (3) (2011) 1721–1734.

[25] J. Wiskin, D. Borup, S. Johnson, M. Berggren, Non-linear inverse scattering: high resolution quantitative breast tissue tomography, The Journal of the Acoustical Society of America 131 (5) (2012) 3802–3813.

[26] Z. Zhang, L. Huang, Y. Lin, Efficient implementation of ultrasound waveform tomography using source encoding, in: Medical Imaging 2012: Ultrasonic Imaging, Tomography, and Therapy, vol. 8320, International Society for Optics and Photonics, 832003, 2012..

[27] J.A. Fessler, Model-based image reconstruction for MRI, IEEE Signal Processing Magazine 27 (4) (2010) 81–89.

[28] J. Verhaeghe, D. Van De Ville, I. Khalidov, Y. D'Asseler, I. Lemahieu, M. Unser, Dynamic PET reconstruction using wavelet regularization with adapted basis functions, IEEE Transactions on Medical Imaging 27 (7) (2008) 943–959.

[29] F. Aguet, D. Van De Ville, M. Unser, Model-based 2.5-D deconvolution for extended depth of field in brightfield microscopy, IEEE Transactions on Image Processing 17 (7) (2008) 1144–1153.

[30] H. Chen, Y. Zhang, M.K. Kalra, F. Lin, Y. Chen, P. Liao, J. Zhou, G. Wang, Low-dose CT with a residual encoder-decoder convolutional neural network, IEEE Transactions on Medical Imaging 36 (12) (2017) 2524–2535.

[31] Y. Han, J.C. Ye, Framing U-Net via deep convolutional framelets: Application to sparse-view CT, IEEE Transactions on Medical Imaging 37 (6) (2018) 1418–1429.

[32] Q. Yang, P. Yan, Y. Zhang, H. Yu, Y. Shi, X. Mou, M.K. Kalra, Y. Zhang, L. Sun, G. Wang, Low-dose CT image denoising using a generative adversarial network with Wasserstein distance and perceptual loss, IEEE Transactions on Medical Imaging 37 (6) (2018) 1348–1357.

[33] I. Häggström, C.R. Schmidtlein, G. Campanella, T.J. Fuchs, DeepPET: A deep encoder-decoder network for directly solving the PET reconstruction inverse problem, arXiv preprint arXiv:1804.07851..

[34] D. Wu, K. Kim, Q. Li, Computationally efficient deep neural network for computed tomography image reconstruction, Medical Physics 46 (11) (2019) 4763–4776.

[35] K. Hammernik, T. Klatzer, E. Kobler, M.P. Recht, D.K. Sodickson, T. Pock, F. Knoll, Learning a variational network for reconstruction of accelerated MRI data, Magnetic Resonance in Medicine 79 (6) (2018) 3055–3071.

[36] W. Shi, F. Jiang, S. Liu, D. Zhao, Image compressed sensing using convolutional neural network, IEEE Transactions on Image Processing 29 (2019) 375–388.

[37] S. Yu, B. Park, J. Jeong, Deep iterative down-up CNN for image denoising, in: Proceedings of the IEEE Conference on Computer Vision and Pattern Recognition Workshops, 2019.

[38] A. Abdelhamed, R. Timofte, M.S. Brown, Ntire 2019 challenge on real image denoising: Methods and results, in: Proceedings of the IEEE Conference on Computer Vision and Pattern Recognition Workshops, 2019.

[39] Y. Lou, W. Zhou, T.P. Matthews, C.M. Appleton, M.A. Anastasio, Generation of anatomically realistic numerical phantoms for photoacoustic and ultrasonic breast imaging, Journal of Biomedical Optics 22 (4) (2017) 041015.

[40] M. Abadi, A. Agarwal, P. Barham, E. Brevdo, Z. Chen, C. Citro, G.S. Corrado, A. Davis, J. Dean, M. Devin, et al., Tensorflow: Large-scale machine learning on heterogeneous distributed systems, arXiv preprint arXiv:1603.04467..

[41] X. Glorot, Y. Bengio, Understanding the difficulty of training deep feedforward neural networks, in: Proceedings of the Thirteenth International Conference on Artificial Intelligence and Statistics, 2010, pp. 249–256.

[42] D.P. Kingma, J. Ba, Adam: A method for stochastic optimization, arXiv preprint arXiv:1412.6980..

[43] O. Ronneberger, P. Fischer, T. Brox, U-net: Convolutional networks for biomedical image segmentation, in: International Conference on Medical Image Computing and Computer-assisted Intervention, Springer, 2015, pp. 234–241..

[44] S. Jégou, M. Drozdzal, D. Vazquez, A. Romero, Y. Bengio, The one hundred layers tiramisu: Fully convolutional densenets for semantic segmentation, in: Proceedings of the IEEE Conference on Computer Vision and Pattern Recognition Workshops, 2017, pp. 11–19.

[45] B. Park, S. Yu, J. Jeong, Densely connected hierarchical network for image denoising, in: Proceedings of the IEEE Conference on Computer Vision and Pattern Recognition Workshops, 2019.

Yuling Fan received her M.E. degree in College of Information Engineering from Northwest A & F University in 2018. She is currently pursuing Ph.D. degree in the Faculty of Mathematics and Computer Sciences of Heidelberg University. Her major research interests include tomographic image reconstruction and deep learning.

Hongjian Wang received the Ph.D. degree in computer science from the Systems and Transportation Labora-tory of the Research Institute on Transportation, Energy and Society, University of Technology of Belfort-Montbéliard, Belfort, France, in 2016. From 2016 to 2019, he was a postdoctoral researcher with the Medical Faculty Mannheim, Heidelberg University, Mannheim, Germany. Since 2020, he has been an associate profes-sor with the School of Computer Science and Technol-ogy, Donghua University, Shanghai, China. His current research focuses on image reconstruction in ultrasound computed tomography.

Hartmut Gemmeke was born in Northeim, Germany, on March 9th, 1944. He studied exp. Physics in Göttin-gen and Heidelberg. Since 1990, he was a supernumer-ary professor at the University of Heidelberg and 1996 at the University of Karlsruhe. Since 2001 he was the director of the Institute for Data Processing and Elec-tronics at KIT. He has about 400 publications including 25 in medical techniques. After his retirement 2010 he is working as scientific advisor at KIT. His present research activities are focused on the investigation of 3D Ultrasound Computed Tomography for early breast cancer recognition.

Torsten Hopp studied applied computer science at the University of Cooperative Education in Mannheim and the University of Heidelberg. He received his BSc. in 2006 and his MSc. in 2009. In 2012 he received his PhD in computer science from University of Mannheim. Since 2003 he is working at Karlsruhe Institute of Technology in the Institute for data processing and electronics. Since 2012 he is a postdoc and senior sci-entist in the Ultrasound Computer Tomography project. His main research interests cover medical imaging with ultrasound tomography, image reconstruction and medical image processing, including model-based image registration.

Juergen Werner Hesser is professor for Data Analysis and Modeling in Medicine at the Mannheim Institute for Intelligent Systems in Medicine (MIISM), Faculty of Medicine Mannheim, Heidelberg University since 2019. Before he was professor for Experimental Radiation Oncology at the same faculty since 2007. Between 2005 and 2007 he was Professor for Medical Technology, Institute of Computer Engineering, University of Man-nheim. He habilitated 1999 in Computer Science, and earned his PhD and Diploma in Physics at Heidelberg University in 1992 resp. 1989. He is co-opted member of the Faculty of Physics and Astronomy and external
member of the Central Institute for Computer Engineering (ZITI), and the Inter-disciplinary Center for Scientific Computing (IWR) where he is member of the board of directors since 2020.